Derivation and Validation of Sensor Brightness Temperatures for Advanced Microwave Sounding Unit-A Instruments

Banghua Yan and Khalil Ahmad

Abstract— In this study, we first present a generalized methodology for deriving sensor brightness temperature data records (SDR) from antenna temperatures data records (TDR) applicable for Advanced Microwave Sounding Unit-A (AMSU-A) instruments. It includes corrections for antenna sidelobe contributions, antenna emission, and radiation perturbation due to the difference of Earth radiance in the main beam and that in the sidelobes that lie outside the main beam but within the earth disc. For practical purposes, we simplify the methodology by neglecting the components other than the antenna sidelobe contributions to establish a consistent formulation with the legacy AMSU-A antenna pattern correction (APC) formula. The simplified formulation is then applied to the final AMSU-A instrument onboard the Metop-C satellite that was launched in November 2018, in order to compute APC coefficients for deriving SDR from TDR data. Further, the performance of the calculated correction coefficients is validated by calculating the differences between the daily averaged AMSU-A (TDR and SDR) observations against radiative transfer model (O-B) simulations under clear sky conditions, and over open oceans. The validation results show that the derived temperature corrections are channel and scan position dependent, and can add 0.2 to 1.6K to the antenna temperatures. In addition, the derived SDR O-B simulation results exhibit a reduced and more symmetric scan angle dependent bias when compared with corresponding TDR antenna temperatures.

***Index Terms*—Microwave Radiometry; AMSU-A Calibration; AMSU-A Antenna Pattern Correction; Metop-C AMSU-A Validation**

I. INTRODUCTION

THE third satellite of the European Meteorological Operational (Metop) satellite program, Metop-C, which was successfully launched into low Earth orbit on November 6, 2018, carries the NOAA Advanced Microwave Sounding Unit-A (AMSU-A) instrument. The AMSU-A provides temperature soundings from the Earth's near-surface to an altitude of about 42 km through measurements of antenna Temperature Data Records (TDR) at 15 channels from 23.8 to 89 GHz.

Table I AMSU-A Instrument Specifications [1]

Ch	Center Frequency (MHz)	Bandwidth (MHz)	Polarization	Measured 3db Beamwidth (°)[1,2]	Measured Main Beam Efficiency[3,4]	Temperature Sensitivity (K) NEΔT
1	23800	270	V	3.48	96.30	0.30
2	31400	180	V	3.52	97.31	0.30
3	50300	180	V	3.64	96.28	0.40
4	52800	400	V	3.40	95.66	0.25
5	53596 ±115	170	H	3.60	96.32	0.25
6	54400	400	H	3.44	96.84	0.25
7	54940	400	V	3.44	96.44	0.25
8	55500	330	H	3.44	96.10	0.25
9	fo= 57290.344	330	H	3.32	96.70	0.25
10	fo ± 217	78	H	3.33	96.70	0.40
11	fo ± 322.2 ± 48	36	H	3.32	96.70	0.40
12	fo ± 322.2 ± 22	16	H	3.32	96.70	0.60
13	fo ± 322.2 ± 10	8	H	3.32	96.70	0.80
14	fo ± 322.2 ± 4.5	3	H	3.32	96.70	1.20
15	89000	1500	V	3.56	97.88	0.50

[1] Specification of 3dB beamwidth is within 3.3°±10%;
[2] 3-dB beamwidth data correspond to beam position 15;
[3] Specification of main beam efficiency is ≥ 95%;
[4] Main beam efficiency is computed using Eq. (6d) with θ_{max} equal to 2.50 x the 3-dB beamwidth in the table.

Table I lists the AMSU-A main channel characteristics, which include the channel frequency, bandwidth (specification and measurements), and radiometric temperature sensitivity (or NEΔT) for each of the 15 channels [1][2]. After a series of calibrations, the AMSU-A TDR data have been distributed to

Manuscript received November 28, 2019, revised on March 27, 2020, and accepted on April 27, 2020. This work was supported by the NOAA Office of Projects, Planning, and Analysis. The manuscript contents are solely the opinions of the authors and do not constitute a statement of policy, decision, or position on behalf of NOAA or the U. S. Government.

B. H. Yan is with the Satellite Calibration and Data Assimilation Branch in the Center for Satellite Applications and Research, National Oceanic and Atmospheric Administration, 5830 University Research Ct, College Park, MD 20740, USA (e-mail: Banghua.Yan@noaa.gov).

K. Ahmad is with the Global Science Technologies Inc., College Park, MD 20742 USA (e-mail: khalil.ahmad@noaa.gov)

the user community through the NOAA OSPO Environmental Satellite Processing and Distribution System (ESPDS) Product Distribution Access (PDA) subsystem and the NOAA Comprehensive Large Array-data Stewardship System (CLASS).

Besides the TDR data, the user community also needs brightness temperature Sensor Data Record (SDR) data, which ideally represents the antenna temperature after corrections of antenna sidelobe contributions [3]-[7], antenna emission [8]-[10], and other radiation perturbations [11]. The conversion from TDR to SDR data has been previously studied, and applied to a number of space-borne radiometers. The radiometers include the Advanced Technology Microwave Sounder (ATMS) instruments onboard the Suomi National Polar-orbiting Partnership (SNPP) and Joint Polar Satellite System (JPSS-1) [8]-[10], and AMSU-A instruments onboard NOAA-15 to 19, and Metop-A & B satellites. While the legacy AMSU-A conversion algorithm [7], only accounted for sidelobe contributions to antenna temperatures due to lack of on-orbit maneuver measurements, the ATMS conversion algorithm contained an additional correction for antenna emission contributions, utilizing data available from deep space pitch-over maneuvers to perform the TDR to SDR corrections [12].

In this study, we take advantage of previous studies and adopt some of their approaches [7] – [13] to formulate a generalized TDR to SDR conversion algorithm for the AMSU-A instruments. In particular, the ATMS emissivity model is utilized to construct the theoretical contribution of the emissive AMSU-A antenna system. No polarized emission measurements were made for the AMSU-A antenna reflector on ground before launch, and there are currently no plans for MetOp-C to perform on-orbit pitch-over maneuvers necessary to derive actual polarized antenna emission. Therefore, we further simplify the generalized theoretical algorithm by ignoring the components other than the contribution from sidelobe radiation, which results in a mathematical formula consistent with the legacy AMSU-A approach. We also adopt the simplified mathematical formula to compute the Antenna Pattern Correction (APC) coefficients for the Metop-C AMSU-A instrument. As was previously demonstrated in [14], we assess the performance of the derived APC conversion coefficients by comparing daily-averaged angular biases of AMSU-A observations with/without APC against simulated brightness temperatures using the Joint Center for Satellite Data Assimilation (JSCDA) Community Radiative Transfer Model (CRTM) [15]-[17].

This paper is organized as follows. After this introduction, the next section provides a brief description of the Metop-C AMSU-A instrument and its antenna pattern data. Section III presents the conversion methodology including the generalized and simplified versions for computing AMSU-A brightness temperatures from measured antenna temperatures. Section IV provides the derived Metop-C AMSU-A APC coefficients along with validations of resultant brightness temperatures. Summary and conclusions are given in the final section.

II. Description of AMSU-A Instrument and Antenna Pattern Data

The Metop-C AMSU-A is composed of two units (A1 & A2), and has three antenna systems, A1-1, A1-2 & A2. The A1-1 system contains channels 6-7 and 9-15; the A1-2 contains channels 3-5 and 8; the A2 system contains channels 1 & 2. Each of these systems consists of an offset parabolic reflector housed in a cylindrical shroud [1]. The antenna reflectors complete one revolution about Y-axis every 8 seconds, during which 30 earth scenes (also referred to as beam positions) within ±48.33° from nadir and each separated by 3.33° are sampled in a stepped-scan fashion, as shown in Fig 1(a) below.

The instrument antenna pattern function (APF) data were measured by the instrument's vendor Northrop Grumman Electronic Systems [1][2]. The APF data were measured at each channel frequency except channels 9–14 that share the same central frequency (57.29 GHz). A geometric sketch of the APF measurement is given via a coordinate system UVW, as displayed in Fig. 1(b). The APF is expressed as $G(\alpha,\gamma)$, i.e., a function of angles α ($=\angle W'SP$) and γ ($=\angle USP'$) relative to the antenna boresight changes with scan angle, where P' is a projection of vector P in the UV plane. For convenience, the α and γ are named as pseudo-view and pseudo-azimuthal angles respectively. Measurements of the APF at each of the ten channel frequencies refer to the determination of the radiation pattern of the tested antenna at different view and azimuthal angles. At each channel, the measured data of the antenna pattern function consist of the following elements.

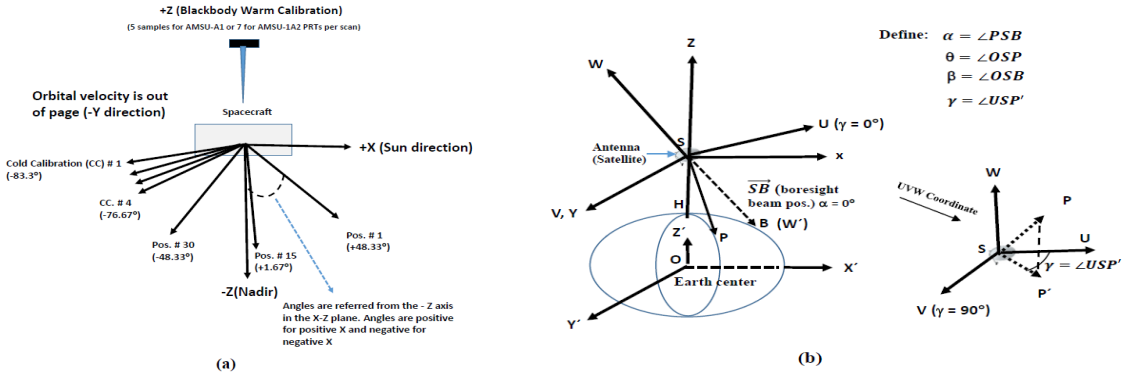

Fig. 1. (a) AMSU-A cross-track scan geometry [2], (b) Geometric sketch of a coordinate system placed at the center of the instrument antenna, the satellite and the earth (revised from [7]). In the figure, the angle α (=$\angle W'SP$) is defined as the angle from the antenna boresight direction while the angle γ ($=\angle USP'$) is a quasi- azimuthal angle, where the boresight is defined to be the central peak of the antenna pattern function.

1) Four planes: at each frequency, antenna pattern data were measured at four plane "cuts". Each cut corresponds to two azimuthal angles (referred to γ), as shown in Fig. 1(b), i.e., $\gamma = 0^{\circ}$and 180°, 45°, and $225°$, 90° and 270°, $135°$ and $315°$, respectively. The plane cuts are hereinafter referred to as the 0, 45, 90, and 135 cuts, respectively.
2) Scanning angular range and interval: The scanning angle (referred to α) extends from 0° to ±180° from each antenna boresight with 0.2° steps, as shown in Fig. 1(b).
3) Fine-step data: For accurate determination of the antenna beam widths, the central parts of the antenna pattern (0° to ±4.5°) were measured at steps of 0.05°. These fine-step data were measured only at two plane cuts, crosstrack ($\gamma = 0^{\circ}$) and downtrack ($\gamma = 90^{\circ}$) cuts, respectively.
4) Three beam positions: Data were taken under three cases where the instrument antenna beam boresight direction points to the beam position # 1, 15, and 30 respectively [see Fig. 1(a)], which were performed by rotating the antenna boresight direction to the required angles. Fig. 1(b) displays the beam position at the beam position 15.
5) Two polarizations: Each set of these antenna patterns was measured with two different polarizations: co-polarizations with identical transmit and receive polarization states and cross-polarizations with transmitting in one polarization state and receiving in the orthogonal polarization state such as VH and HV, where 'H' denotes the horizontal polarization and 'V' the vertical polarization.

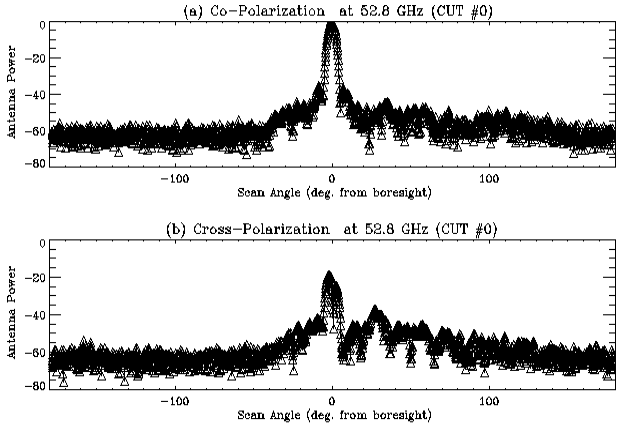

Fig. 2. Channel 4 antenna pattern functions of both co-polarization in (a) and cross-polarization in (b) at the plane cut 0° (azimuthal angle of 0°) and for beam position 1. Both co-polarized and cross-polarized data were normalized relative to the boresight peak of co-polarization.

Figure 2 shows an example of the Metop-C AMSU-A channel 4 (52.8 GHz) APF data at the plane cut 0 and beam position 1 for both co-polarization in (a) and cross-polarization in (b). As can be seen from the figure, the cross-polarization spectra are approximately 20 dB smaller than the corresponding ones in co-polarization in the main lobe. However, the cross- and co-polarized power signals in the sidelobes at large scan angles have about the same magnitudes.

In the following section, we describe the methodology utilized for the deriving the AMSU-A SDR from the TDR data.

III. Methodology for Deriving AMSU-A SDR from TDR Data

For an emissive microwave antenna with radiation efficiency ξ_{Ref}^{p}, the antenna temperature T_A^p, which is the energy received by the antenna as it is used to observe radiation from a target with brightness temperature of T_B^p, consists of two parts, one representing the received energy by the antenna through the main beam and sidelobes, the other representing the noise power of the antenna [7] and [13]

$$T_A^p = \xi_{Ref}^{p}\left[\frac{\iint_{mainbeam} T_B^p(\alpha,\gamma)\, G(\alpha,\gamma)d\Omega}{\iint_{4\pi} G(\alpha,\gamma)d\Omega} + \frac{\iint_{4\pi-mainbeam} T_B^p(\alpha,\gamma)\, G(\alpha,\gamma)d\Omega}{\iint_{4\pi} G(\alpha,\gamma)d\Omega}\right] + \left(1-\xi_{Ref}^{p}\right)T_{Ant}, \quad (1)$$

where the superscript 'p' denotes hereinafter vertical ('V') and horizontal ('H') polarization states unless otherwise described; T_{Ant} is the physical temperature of the antenna. The parameter $G(\alpha,\gamma)$ denotes the antenna pattern function that varies with angles α and γ relative to the antenna boresight changes with scan angle at the coordinate placed at the center of the antenna [see Fig. 1(b)]. The quantity ξ_{Ref}^{p} denotes the ratio of the total power reflected by an antenna to the net power accepted by the antenna [13]. Therefore, (1) implies that an emissive antenna with $\xi_{Ref}^{p} < 1$ not only delivers less signal power to the receiver, but also contributes noise power of its own.

By applying the above principle to a spaceborne instrument, the energy received by the antenna, i.e., the items of the bracket in (1), can consist of more components. In this study, we consider the following four radiation components, i.e., the contributions from the Earth radiation via the antenna main beam, the Earth radiation via the antenna sidelobes that are out of the main beam but within the Earth view sector, the cold space radiation via the antenna sidelobes, the spacecraft radiation via the antenna sidelobes. For clarity, in the following analysis, the subscript 'me', 'se', 'sc', and 'ss' are employed to distinguish similar parameters relating to the above four sources, i.e., the main beam from the Earth (me), the sidelobes from the Earth (se), the sidelobes from the cold space (sc), and the sidelobes from the spacecraft (ss).

Additionally, for a cross-track scanning microwave radiometer such as AMSU-A or ATMS, pure vertical or horizontal polarization measurements (T_A^p) only occur at the nadir direction. At the other beam positions (β), the satellite measurements actually represent a mixed contribution from both V and H polarizations, which are defined as the quasi-vertical and quasi-horizontal antenna brightness temperature

respectively [10], i.e., $T_A^{Q_p}$ with p = v or h. The formulas of $T_A^{Q_p}$ had been developed under certain approximations for either AMSU-A or ATMS [7][8][10]. In this study, we take advantage of these studies and adopt some of their results to establish the generalized methodology for AMSU-A instruments, as described below.

Following the convention in [7], also depicted in the geometric sketch provided in Fig. 1(b), a number of coordinate systems are introduced. The first is the XYZ system attached to the Satellite (S) flying at height H (~ 832 km for Metop-C) above the earth's surface. A second coordinate system X`Y`Z`, which is parallel to the first system, is placed at the earth's center, where the AMSU-A antenna boresight is assumed to scan crosstrack in the *X′Z′*–plane to acquire data at 30 earth views, cold space, and the blackbody target, respectively. The third system (UVW) which is also attached to the satellite and useful for performing integrations involving antenna pattern function data.

The $T_A^{Q_p}$, with p = v or h, are expressed and computed in the Cartesian coordinate system *X′Y′Z′* placed at the earth's center. By utilizing equation (1) and legacy studies [7]-[10], we derive the formulas of $T_A^{Q_p}$ and summarize them below (See Appendix A for details).

$$T_A^{Q_v} = \xi_{Ref}^v\{[(\eta_{me}^{vv} + \eta_{se}^{vv}) + (\eta_{me}^{hv} + \eta_{se}^{hv})]T_B^{Q_v} + (\eta_{sc}^{vv} + \eta_{sc}^{hv})T_C + S_a^{Q_v}\} + (\Delta T_A^{Q_v})', \quad (2a)$$

$$T_A^{Q_h} = \xi_{Ref}^h\{[(\eta_{me}^{hh} + \eta_{se}^{hh}) + (\eta_{me}^{vh} + \eta_{se}^{vh})]T_B^{Q_h} + (\eta_{sc}^{hh} + \eta_{sc}^{vh})T_C + S_a^{Q_h}\} + (\Delta T_A^{Q_h})', \quad (2b)$$

with

$$(\Delta T_A^{Q_v})' = \xi_{Ref}^v\left[(A^h - 1.0)(\eta_{me}^{hv} + \eta_{se}^{hv})T_B^{Q_v} + (\eta_{se}^{vv} + \eta_{se}^{hv})(E_B^{Q_v} - T_B^{Q_v}) + (A^h - 1)\eta_{se}^{hv}(E_B^{Q_v} - T_B^{Q_v})\right], \quad (3a)$$

$$(\Delta T_A^{Q_h})' = \xi_{Ref}^h\left[(A^v - 1.0)(\eta_{me}^{vh} + \eta_{se}^{vh})T_B^{Q_h} + (\eta_{se}^{hh} + \eta_{se}^{vh})(E_B^{Q_h} - T_B^{Q_h}) + (A^v - 1)\eta_{se}^{vh}((E_B^{Q_h} - T_B^{Q_h})\right], \quad (3b)$$

$$S_a^{Q_v} = C_0 + C_1\, sin^2\theta, \quad (3c)$$

$$S_a^{Q_h} = C_0 + C_1\, cos^2\theta, \quad (3d)$$

$$C_0 = \left[\sigma\xi_{Ref}^v(\eta_{ss}^{vv} + \eta_{ss}^{hv}) + \left(1 - \xi_{Ref}^v\right)\right]T_{SAT}, \quad (3e)$$

$$C_1 = \{\sigma(\xi_{Ref}^h\eta_{ss}^{hh} - \xi_{Ref}^v\eta_{ss}^{vv}) + \sigma\left(\xi_{Ref}^h\eta_{ss}^{vh} - \xi_{Ref}^v\eta_{ss}^{hv}\right) + \left(\xi_{Ref}^v - \xi_{Ref}^h\right)\}\, T_{SAT}. \quad (3f)$$

where brightness temperatures are assumed to be homogeneous within relevant solid angles. The definitions of the various variables in equations above are briefed in Table II. The scale factor σ is introduced into η_{ss}^{pp} and η_{ss}^{qp} to account for the approximation of near-field effect of the satellite platform because of the use of the far-field pattern function data [7][18] (also refer to Appendix A). Note that the $T_A^{Q_p}$ and other radiation variables in the expressions are functions of instrument channel frequency υ and scan angle β, but these indices are typically omitted for clarity.

Equations (2a) and (2b) represent the generalized formulas of AMSU-A-measured antenna temperatures for a lossy antenna. It includes Earth radiation entering into the receiver system through the main beam and the sidelobes, the cold-space radiation through the sidelobes, the radiation emitted from satellite platform in the near-field through the sidelobes, as well as antenna emission. It also contains the radiation perturbation due to the difference of Earth radiance in the main beam and that in the sidelobes that lie outside the main beam but within the earth disc. The newly derived expressions are very similar to those in [8] for ATMS except for the effect of antenna noise radiation, i.e., the radiation with $\left(1 - \xi_{Ref}^v\right)$ in (3e).

Table II Explanations of the variable in (2a) through (3f)

Variable	Explanations
$T_B^{Q_p}$	Quasi-vertical (*p*=*v*) or -horizontal (*p*=*h*) brightness temperature of the Earth scene illuminated by the main beam
$E_B^{Q_p}$	Quasi-vertical (*p*=*v*) or quasi-horizontal (*p*=*h*) brightness temperature of the Earth seen by the antenna sidelobes that are out of the main beam but within the Earth view sector
T_C	Brightness temperatures of the cold space seen by the sidelobes
T_{SAT}	Brightness temperature of the antenna on the satellite
$S_a^{Q_p}$	Quasi-vertical (*p*=*v*) or quasi-horizontal (*p*=*h*) radiation emitted from the satellite platform in the near-field as well as antenna emission
A^p	An empirical parameter representing a correlation between $T_B^{Q_v}$ and $T_B^{Q_h}$ as a function of scan angle, which is used in the cross-polarized efficiency item
η_x^{pp}(x=me, se, sc, or ss)	Co-polarized antenna efficiencies respectively via a specific solid angle Ω_x subtended by the antenna main beam (m) or the sidelobes (s) that intersect with Earth (e) or cold space (c) or spacecraft platform (s)
η_x^{qp}	Same as η_x^{pp} except for cross-polarized antenna efficiencies

For all radiation-related items except for the satellite cross-radiation item in the above equations, approximately assume that $\eta_x^{vv} = \eta_x^{hh} = \eta_x^{co}$ and $\eta_x^{vh} = \eta_x^{hv} = \eta_x^{cross}$, with $x = me, se, sc\ and\ ss$. Equations (2a) and (2b) are thus standardized into the following expressions to provide a connection to the legacy AMSU-A APC algorithm:

$$T_A^{Q_p} = [f_E T_B^{Q_p} + f_C T_C + f_{SAT}\sigma T_{SAT}] + \Delta T_A^{Q_p} \quad (4)$$

with

$$\Delta T_A^{Q_p} = (\Delta T_A^{Q_p})_{Ref} + (\Delta T_A^{Q_p})_{ETem} + (\Delta T_A^{Q_p})_{EPol}. \quad (5a)$$

$$(\Delta T_A^{Q_p})_{Ref} = \left(\xi_{Ref}^p - 1\right)\left[f_E T_B^{Q_p} + f_C T_C + f_{SAT}\sigma T_{SAT}\right] + \left(1 - \xi_{Ref}^p\right)T_{SAT} + (\Delta T_A^{Q_p})_{Ref}^{Cross}, \quad (5b)$$

$$\left(\Delta T_A^{Q_p}\right)_{ETem} = \xi_{Ref}^p f_{se}\left(E_B^{Q_p} - T_B^{Q_p}\right) + (A^q - 1)f_{se}^{cross}(E_B^{Q_p} - T_B^{Q_p}), \quad (5c)$$

$$(\Delta T_B^{Q_p})_{EPol} = \xi_{Ref}^p(A^q - 1.0)f_E^{cross}T_B^{Q_p}, \quad (5d)$$

$$(\Delta T_A^{Q_v})_{Ref}^{Cross} = C_1\, cos^2\theta, \quad (5e)$$

$$(\Delta T_A^{Q_h})_{Ref}^{Cross} = C_1\, sin^2\theta. \quad (5f)$$

The variables in the above equations related to antenna efficiencies are explained in Table III, but their calculation formula are given in Section IV.B. Other variables are given in Table II.

Notice that the items in the bracket in (4) are the same as that in the legacy AMSU-A algorithm in [7]. The quantity $\Delta T_A^{Q_p}$ represents the deviation in deriving brightness

temperatures using the legacy APC algorithm from that using the generalized algorithm in (4). It consists of three types of radiation perturbations due to AMSU-A reflector emission ($(\Delta T_B^{Q_p})_{Ref}$), Earth scene temperature heterogeneity effect $[(\Delta T_B^{Q_p})_{ETem}]$, and Earth radiation polarization $[(\Delta T_B^{Q_p})_{EPol}]$.

Table III Descriptions of several antenna efficiencies in (4) to (5f)

Variable	Description
f_E	$f_{me} + f_{se}$, antenna efficiency subtended by earth
f_{me}	$\eta_{me}^{co} + \eta_{me}^{cross}$, antenna main beam efficiency by earth
f_{se}	$\eta_{se}^{co} + \eta_{se}^{cross}$, antenna sidelobe efficiency by earth
f_C	$\eta_{sc}^{co} + \eta_{sc}^{cross}$, antenna sidelobe efficiency by cold space
f_{SAT}	$\eta_{ss}^{co} + \eta_{ss}^{cross}$, antenna sidelobe efficiency by satellite platform

As explained earlier, due to lack of sufficient information about the AMSU-A instrument antenna to compute $\Delta T_A^{Q_p}$, it is difficult to accurate compute each component in (5b) through (5f). It is more vital to provide the user community with the conversion coefficients for Metop-C AMSU-A instrument consistent with the legacy AMSU-A instruments. Therefore, we further make the following assumptions:

1) Earth radiation is non-polarized in the cross-polarized antenna efficiency item, i.e., $A^h = A^v = 1.0$;
2) Earth radiation within viewing field via the antenna main beam and sidelobes is uniform, i.e., $E_B^{Q_v} = T_B^{Q_v}$ and $E_B^{Q_h} = T_B^{Q_h}$.
3) AMSU-A antenna reflector is lossless, i.e., $\xi_{Ref}^v = \xi_{Ref}^h = 1.0$;
4) For both far- and near-field radiations, $\eta_x^{vv} = \eta_x^{hh} = \eta_x^{pp}$ and $\eta_x^{vh} = \eta_x^{hv} = \eta_x^{pq}, with\ x = me, se, sc\ or\ ss.$

With those assumptions, the quantity $\Delta T_A^{Q_p}$ disappears, so (4) is simplified to the formula consistent with the legacy AMSU-A APC algorithm [7]. Through the normalization of the efficiencies, we established the following simplified APC algorithm.

$$T_A^{Q_p}(\beta) = \frac{1}{N_\sigma}[f_E(\beta)T_B^{Q_p} + f_C(\beta)T_C + f_{SAT}(\beta)\sigma T_{SAT}], \qquad (6)$$

where the scan angle β is included to highlight the variation of $T_A^{Q_p}(\beta)$ with beam position. The contribution of energy by each radiation component is normalized by a scale factor N_σ, where $N_\sigma = f_E(\beta) + f_C(\beta) + f_{SAT}(\beta)\sigma$.

In the next section, we use the simplified formulas to derive brightness temperatures from antenna temperatures for Metop-C AMSU-A instrument.

IV. TDR to SDR Conversion Coefficients for Metop-C AMSU-A

In this section, we first utilize the measured antenna pattern data to calculate the 3-dB beamwidths and main beam efficiencies for the MetOp-C AMSU-A channels to ensure that the instrument meets the design specifications [1][2]. Next, we employ the antenna pattern data along with the formulation developed in Section III to derive the antenna pattern correction (APC) coefficients (also known as antenna efficiencies) to perform the conversion from TDR measurements to sensor brightness (SDR) temperatures. The calculation of antenna efficiencies over three solid angle regions subtended at the satellite by the earth, cold space, and satellite platform are performed at 30 beam positions for all AMSU-A channels. Finally, the accuracy of the derived brightness temperatures using calculated coefficients is assessed through comparisons to radiative transfer model simulations.

A. Beamwidths and Main Beam Efficiencies

For a given antenna pattern function at a given plane "cut", as displayed in Fig. 2, the 3-dB beamwidth is defined as the full angular width between two antenna view angles (α), which are prescribed by the points on the antenna pattern where its magnitude drops to one-half of its peak value at boresight. For a given beam position, each of the 3-dB beamwidths is the average value of those obtained from the crosstrack cut ($\gamma = 0°$) and downtrack cut ($\gamma = 90°$) measurements of the fine-step (0.05°) antenna pattern data. Specifically, the 3-dB beamwidths of AMSU-A channels were calculated at three beam positions (1, 15, and 30) using the fine step (0.05°) co-polarized antenna pattern data measurements. These fine-step measurements were taken near the central part (±4.5°) of the antenna pattern data at the crosstrack (γ=0°) and downtrack (γ=90°) plane cuts. Linear interpolation of fine step data was used to determine the exact half-power (3-dB) locations for both cuts.

The results show that all calculated channel 3-dB beamwidths at the three beam positions (1, 15 and 30) are within specification (3.3° ±10%). The channel 3-dB beamwidth values reported in Table I represents the average value of those obtained from the crosstrack and downtrack fine step measurements at beam position 15. It should be noted that our calculations of the AMSU-A channel 3-dB beamwidth values were in very good agreement with values calculated by the instrument vendor & reported in the calibration book [18]. In Table I, the beamwidths at channels 10 to 14 are assumed to be the same as that of channel 9, since they all share the same antenna pattern data.

Utilizing the 3-dB beamwidths in Table I, we further calculated the main beam efficiencies using formulations in [7] that are also briefed in the following sub-section. The calculated results at beam position 15 are listed in Table I. The AMSU-A specification requires that the main beam efficiencies at least 95% for all channels. Thus, the results show that the Metop-C AMSU-A instrument also meets the specifications regarding main beam efficiency at all channels since all of calculated values are above the 95% requirement.

B. Antenna Efficiencies

For consistency with the legacy AMSU-A formulation [9], we calculate the antenna pattern efficiencies over three solid angle regions subtended at the satellite by the earth (and atmosphere below 20 km), cold space, the satellite platform, which are denoted by $f_E(\beta)$, $f_C(\beta)$, and , $f_{SAT}(\beta)$, respectively. For each antenna beam position (β), the three efficiencies are computed by performing integrations of the channel antenna

pattern co-polarized & cross-polarized data components over appropriate solid angle limits corresponding to each region [7].

The co-polarized & cross-polarized antenna efficiencies are defined in [7] and are briefed here:

$$\eta_x^{pp} = \frac{1}{N}\int_{\Omega_x} G^{Co}(\alpha,\gamma)d\Omega, \quad (7a)$$

$$\eta_x^{qp} = \frac{1}{N}\int_{\Omega_x} G^{Cross}(\alpha,\gamma)d\Omega, \quad (7b)$$

$$N = \int_{4\pi}\left(G^{Co}(\alpha,\gamma) + G^{Cross}(\alpha,\gamma)\right) d\Omega, \quad (7c)$$

where the solid angle Ω_x (x = E, C, SAT) limits corresponds to one for earth, cold space, or satellite platform, respectively. For each beam position, the total antenna efficiency is computed as the sum of the co-polarized & cross-polarized components

$$f_x = \eta_x^{pp} + \eta_x^{qp}, \quad (8)$$

where we assume that $\eta_x^{pp} = \eta_x^{Co}$, and $\eta_x^{qp} = \eta_x^{Cross}$.

As noted previously, and shown in Fig. 1, the angles α and γ constitutes the spherical angles around the boresight direction in the UVW coordinate system. These values are used to determine the antenna pattern function values in the integrations, and they can be expressed as a function of θ, ϕ, and β in the XYZ coordinate system by using the following formulas [7]:

$$\alpha = cos^{-1}(sin\beta\ sin\theta\ cos\phi + cos\beta\ cos\theta) \quad (9a)$$

$$\gamma = tan^{-1}\left(\frac{sin\theta\ sin\phi}{cos\beta\ sin\theta\ cos\phi - sin\beta\ cos\theta}\right) \quad (9b)$$

For a given beam position (β), the above equations provide a one-to-one correspondence between (α,γ) and (θ,ϕ), so we can write the corresponding antenna efficiencies as:

$$f_x\ (\beta) = \frac{1}{N}\int_{\theta_x} g(\theta)sin\theta d\theta \quad (10)$$

Where

$$g(\theta) = \int_0^{2\pi}(G^{Co}(\alpha,\gamma) + G^{Cross}(\alpha,\gamma))d\phi \quad (11)$$

As noted earlier, for the calculation of the earth efficiency term, $f_E(\beta)$, the legacy AMSU-A algorithm extends the corresponding solid angle region to include the atmosphere below 20km above the earth surface, therefore, the upper integration limit θ_{max} is traditionally calculated using formula

$$\theta_{max} = sin^{-1}\left(\frac{R+20}{R+h}\right) \quad (12)$$

where R (~ 6371.2 km) is the earth's radius, and h (~ 832 km) is height of satellite. It should be noted that conservation of energy requires $f_E(\beta) + f_c(\beta) + f_{SAT}(\beta) = 1$ for any given beam position (β) value.

We use the above formulas to calculate the three efficiency values at 30 beam positions for all AMSU-A channels, where antenna pattern data are available. The calculated efficiency values can be made available to interested users upon request.

According to the results of three efficiency computations, the earth $f_E(\beta)$ efficiency term accounts for ~99% of the energy reaching the antenna. In contrast, the total contribution from both the cold space and satellite spacecraft radiation is on the order of ~ 1%. The computation results also show that efficiencies are also frequency and scan-angle dependent somewhat asymmetric with respect to nadir. For example, the efficiencies computed for the Earth region vary from near-nadir to edge beam positions by 0.2% to 0.5%, depending on the channel. The difference from the left to right margin beam positions has a magnitude only up to 0.2%. The behavior of the calculated efficiencies for cold space show an opposite asymmetric feature, which is expected due to conservation of energy, as discussed earlier.

This is expected since the summation of the three efficiency components from Earth, cold space and satellite is unity, and the contribution from the satellite in the simplified algorithm is unity as mentioned above.

For demonstration, Fig. 3 displays f_E, f_C and f_{SAT} at channel 4 as a function of beam position. Three antenna efficiencies exhibit a slight dependency on beam position: channel 4 has the largest antenna efficiency (0.9976) at the beam position 15 (close to the nadir direction); it decreases to 0.9927 and 0.9915 at the beam position 1 and 30 respectively, demonstrating certain asymmetrical pattern. In the figure, the antenna efficiency over the regions subtended by the satellite is not weighted by the near-field effect (σ). As it is taken into account, the contribution of the satellite radiation via the sidelobes is negligible since the magnitude of σ is less than 0.11 for all channels [7].

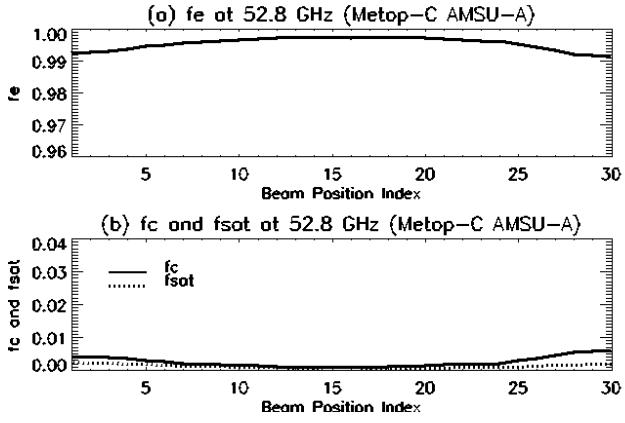

Fig. 3. Metop-C AMSU-A Antenna efficiencies f_E, f_C and f_{SAT} vs. beam position (index) for channel 4. (a) f_E. (b) f_C and f_{SAT}.

In addition, the efficiencies are slightly frequency-dependent, but this dependency changes with the scan beam position (the figure is omitted). For example, at the beam position 15 (close to the nadir direction), the channel 7 exhibits the largest antenna efficiency (0.9988) whereas the channel 15 has the smallest one

(0.9896); at the beam position 30, the channel 15 exhibits the largest antenna efficiency (0.9963) whereas the channels 3 and 7 have the smallest one (0.9929).

C. Derivations of Brightness Temperatures

Using the three antenna efficiency values $f_E(\beta)$, $f_C(\beta)$ and $f_{SAT}(\beta)$ calculated in the previous section, we can determine the conversion from Earth antenna (T_A^{Qp}) temperatures to sensor brightness temperatures (T_B^{Qp}).-By re-arranging (6), we have

$$T_B^{Qp}(\beta) = \alpha_0(\beta) T_A^{Qp}(\beta) - \alpha_1(\beta) \qquad (13)$$

with

$$\alpha_0(\beta) = 1.0 + \frac{f_C(\beta)}{f_E(\beta)} + \frac{\sigma f_{SAT}(\beta)}{f_E(\beta)}, \qquad (14a)$$

$$\alpha_1(\beta) = \frac{f_C(\beta) T_C + \sigma f_{SAT}(\beta) T_{SAT}}{f_E(\beta)}. \qquad (14b)$$

The value of T_{SAT} or the temperature of the reflector is not measured for Metop-C and other legacy AMSU-A instruments. Usually it is replaced by Radio Frequency (RF) shelf temperature that is measured onboard. For Metop-C AMSU-A, three RF temperatures are measured corresponding to the sub-systems A1-1 (channels 6-7, 9-15), A1-2 (the channels 3-5 and 8) and A2 (channels 1 and 2) respectively. The magnitudes for the same antenna change with location and time, and their daily means are monitored in the NOAA Integrated Calibration and Validation System (ICVS) (https://www.star.nesdis.noaa.gov/icvs/status_MetOPC_AMSUA.php). In this study, we assume that T_{SAT} = 286.5, 287.5, 294.5K for the three antennas respectively.

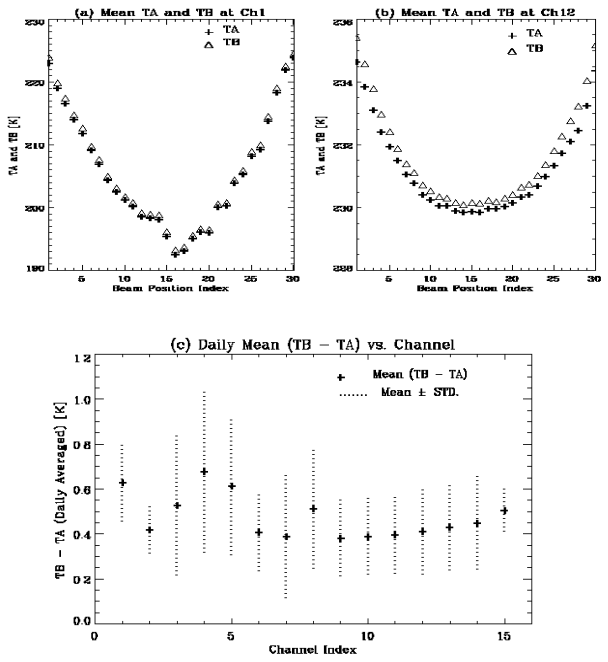

Fig. 4. Comparison of antenna (T_A) and brightness (T_B) temperatures and the differences by using the Metop-C AMSU-A SDR data on June 1, 2019. TB is computed using the simplified APC algorithm as shown in Eqs. (6) through (7). (a) Comparison of Daily averaged TA and TB in the channel 1. (b) Same as (a) except for the channel 2. (c) Daily averages of ($T_B - T_A$) vs. channel.

Using on Metop-C AMSU-A TDR data on June 1, 2019 as an example, we computed T_B from T_A via the above equations. In view the computation results at all channels, both T_A and T_B at the 15 AMSU-A channels show a strong angle dependent feature due to the limb effects towards the two ends of the scanning swath resulting from changes in the optical path-length through the Earth's atmosphere between the Earth and the satellite [19]. They also exhibit certain asymmetry features with angle in the two sides relative to the nadir (beam position 15). Figs. 4(a) and 4(b) display daily averaged antenna and brightness temperatures at the channels 1 (window) and 12 (upper sounding). Compared to T_A, T_B has reduced asymmetry features with scan angle. This is understandable because the asymmetrical integrated efficiencies from the Earth and cold space components have partially mitigated the asymmetric feature of antenna temperatures. In addition to the angle dependence features of T_A and T_B, the magnitudes of corrected temperatures (i.e., $T_B - T_A$) due to antenna efficiencies using (7) are also important, varying approximately between 0.2 K and 1.6K depending on channel and beam position with the largest correction near end of swath. As an example, Fig. 4c displays the averaged $T_B - T_A$ and the standard deviations vs. channel using the same data sets as the above. The averaged corrections range from 0.4 and 0.7 K with the standard deviation of from 0.1 to 0.4K depending on channel. The standard deviation is caused mainly due to changes in beam position and antenna (brightness) temperature.

D. Comparison of Antenna and Brightness Temperatures against CRTM Simulations

To further validate the performance of the derived APC coefficients, we compare the angular distributions of AMSU-A observations with/without APC against radiative transfer model simulations. The AMSU-A observations represent either antenna temperatures (TDR) or brightness temperatures (SDR) derived using the calculated antenna efficiencies. The model simulations are computed using the Joint Center of Satellite Data Assimilation (JCSDA) Community Radiative Transfer Model (CRTM) [15]-[17] along with collocated European Centre for Medium-Range Weather Forecasts (ECMWF) surface conditions and atmospheric profiles. We use the ECMWF analysis data as they are well validated against numbers of radiosonde measurements, with a bias within one Kelvin at levels from 100 through 1000 hPa [20][21]. The computed data is only over oceans under clear skies for both window and sounding channels. A legacy algorithm for estimating cloud liquid water over oceans [22] is employed to calculate liquid water content (LWC) over oceans. The data with LWC larger than 0.1 mm is considered under cloudy conditions. To produce consistent data sets between the observations and the simulations, the above mentioned cloud filter is also applied to the simulated data set.

According to our computation results, at sounding channels 4 to 14, Metop-C AMSU-A brightness temperatures, compared to uncorrected antenna temperatures, exhibit a reduced and more uniform scan dependent bias across the measurement swath (beam position) against CRTM simulations. However, at three window channels, i.e., channels 1, 2 and 15, and dirty

window channel 3, the angular dependent bias pattern with the APC (brightness temperatures) remains similar as that without APC (antenna temperatures). Such bias features are primarily due to uncertainties of CRTM simulations since corresponding simulation accuracies are extremely sensitive to the error of surface emissivity errors [23].

Figure 5(a) and (b) show the daily-mean angular-dependent differences between Metop-C AMSU-A observations (O) and CRTM simulations (B) at channels 5 and 15 respectively. At the sounding channel 5, brightness temperature biases are within -0.5K except for the large beam positions close to the cold space positions where the biases are around -1K. In opposite to this, antenna temperature biases at the same channel are beyond -0.5K. They also have strong satellite view angle dependency and asymmetric feature where the biases vary from -1.15K on the right margin side (small beam position Indies) to -2.46K on the left margin side (large beam position indies). Figs. 5(c) and 5(d) further display the daily averages (all available locations and beam positions) of (O – B) and their standard deviation vs. channel for T_A in (c) and T_B in (d). Overall, smaller biases remain in brightness temperatures than antenna temperatures for all channels except for window channels where a similar bias is observed. Relativly large standard deviations at window channels are primarily due to uncertainties in CRTM simulations. Similar features are observed by applying the APC coefficients to different days of the AMSU-A TDR data (https://www.star.nesdis.noaa.gov/icvs/).

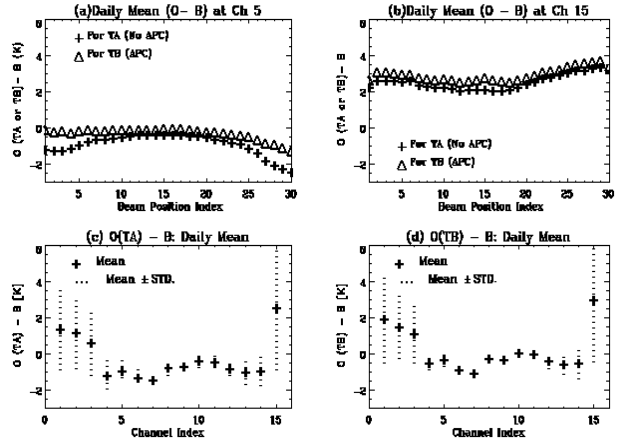

Fig. 5. Daily mean differences between Metop-C AMSU-A observations (O) (T_A *or* T_B) and RTM simulations (B) under clear skies over oceans by using the SDR data on June 1, 2019. T_B is computed from T_A using the simplified APC algorithm as shown in Eqs. (6) through (7). (a) Angular dependent daily mean (O – B) in the channel 5 vs. beam position. (b) Same as (a) except for the channel 15. (c) Daily averages of O (T_A) – B vs. channel. (d) Daily averages of O (T_B) – B vs. channel.

Overall, the derived APC coefficients have demonstrated good performance in both deriving brightness temperatures and improving the asymmetrical bias features at the most of the channels against the CRTM simulations. Currently, the derived APC coefficients have been delivered to a series of operational users, including but not limited to the NOAA Microwave Integrated Retrieval System (MIRS) (https://www.star.nesdis.noaa.gov/mirs/), the NOAA Unique Combined Atmospheric Processing System (NUCAPS), NOAA Environmental Modeling Center (EMC), European Organisation for the Exploitation of Meteorological Satellites (EUMETSAT), USA Naval Research Laboratory (NRL), European Centre for Medium-Range Weather Forecasts (ECMWF), and ATOVS and AVHRR Pre-processing Package (AAPP).

V. Summary and Conclusions

In this study, we have established a generalized methodology for deriving Earth sensor brightness temperature (SDR) from antenna temperature (TDR) data for AMSU-A instruments by taking advantage of previous studies [7]-[13]. This methodology takes into the account corrections of several major perturbation radiation components resulting from the following mechanisms: cold space and satellite platform radiation sensed by the antenna sidelobes; direct antenna radiance emission; radiation due to Earth scene radiance heterogeneity between the regions inside the antenna main beam and the sidelobe regions outside the main beam but within the Earth view sector; and window channel radiation associated with cross-polarized antenna efficiencies due to vital Earth radiation polarization differences.

To comply with the legacy AMSU-A SDR method [7] and also due to lack of sufficient measurements, however, we further simplify the generalized algorithm by disregarding the influences of the components other than the cold space and spacecraft antenna sidelobe contributions to establish a conversion procedure determined only by the APC coefficients for Metop-C AMSU-A. This simplified formula is employed to compute APC coefficients for the Metop-C AMSU-A instrument. The performance of the derived coefficients has been validated by applying them to the Metop-C AMSU-A TDR data on June 1, 2019. Compared to antenna temperatures in the TDR data, the resulting brightness temperatures demonstrate reduced scan angle dependent artifacts. The magnitudes of corrected temperatures (i.e., $T_B - T_A$) vary approximately between 0.2 K and 1.6K depending on channel and beam position with the largest correction near end of swath beam positions. This feature is also observed in the daily averaged biases of brightness temperatures against the CRTM simulated brightness temperatures. The brightness temperatures (with APC) typically exhibit a more uniform scan-dependent bias compared to antenna temperatures (no APC). At the sounding channel 5, brightness temperature biases are within -0.5K except for the large beam positions close to the cold space positions where the biases are around -1.0K. In opposite to this, antenna temperature biases at the same channel are typically – below -1.0K, where the biases vary from -1.15K on the right margin side to -2.46K on the left margin side (large beam position indies). Further results from additional days can be found on the STAR ICVS website (https://www.star.nesdis.noaa.gov/icvs/).

Metop-C AMSU-A SDR data that are converted from TDR data via the APC coefficients display a good quality and have

passed the final STAR internal calibration and validation review [24], declaring the Metop-C AMSU-A data ready for operational use. However, residual biases remain at all channels in the brightness temperatures against the CRTM simulated values. Particularly, the biases are strongly asymmetric angle dependence and those towards the two ends of the scanning swath are low as -2.0 K at some sounding channels. CRTM simulations have relatively large uncertainties at window channels and lower sounding channels. A few radiation perturbation components could contribute to the residual biases, which are neglected in the simplified algorithm, e.g., antenna emission and heterogeneity effect due to the difference of Earth radiation in the different viewing solid angles. In addition, possible instrument polarization misalignment might be an additional cause for the asymmetric feature [25]. Impacts of those uncertainties on the accuracy of derived brightness temperatures will be examined by using the generalized methodology in a separate study to further improve the SDR data quality.

Appendix A Derivation of Generalized AMSU-A APC Formulas

For a lossy microwave antenna with radiation efficiency ξ_{Ref}^{p}, the antenna temperature T_A, which is the energy received by the antenna as it is used to observe radiation from a target with brightness temperature of T_B, consists of two parts, one representing the received energy by the antenna through the main beam and sidelobes, the other representing the noise power of the antenna [7][13]

$$T_A^p = \xi_{Ref}^p \left[\frac{\iint_{mainbeam} T_B(\alpha,\gamma)\, G(\alpha,\gamma) d\Omega}{\iint_{4\pi} G(\alpha,\gamma) d\Omega} + \frac{\iint_{4\pi-mainbeam} T_B(\alpha,\gamma)\, G(\alpha,\gamma) d\Omega}{\iint_{4\pi} G(\alpha,\gamma) d\Omega} \right] + \left(1 - \xi_{Ref}^p\right) T_{Ant}, \quad \text{(A1)}$$

where T_{Ant} is the physical temperature of the antenna; the superscript 'p' denotes vertical (referred to 'V') and horizontal (referred to 'H') polarization states unless otherwise described. The $G(\alpha,\gamma)$ denotes the antenna pattern function that varies with the zenith angle α and azimuthal angle γ of the antenna boresight direction relative to the nadir at the coordinate placed at the center of the antenna (see Fig. 2). The quantity ξ_{Ref}^{p} denotes the ratio of the total power radiated by an antenna to the net power accepted by the antenna [13]. For a lossy antenna with $\xi_{Ref}^{p} < 1$, it not only delivers less signal power to the receiver, but also contributes noise power of its own.

By applying (A1) to a spaceborne instrument such as AMSU-A, the first item of this equation can consist of radiative energies from the Earth and other targets via the antenna within the main beam and sidelobes. These targets include spillover directly from space, spillover emission from the spacecraft, reflector emission, sensor emission, etc., through either the antenna main beam or the sidelobes. In this study, we only consider the following four sources, i.e., the contributions from the Earth radiation via the antenna main beam, the Earth radiation via the antenna sidelobes that lie out of the main beam but within the Earth view sector, the cold space radiation via the antenna sidelobes, and the spacecraft radiation via the antenna sidelobes. For clarity, in the following analysis, the subscript 'me', 'se', 'sc', and 'ss' are employed to distinguish similar parameters relating to the above four sources, i.e., the main beam from the Earth, the sidelobes from the Earth, the sidelobes from the cold space, and the sidelobes from the spacecraft respectively. In addition, we assume that brightness temperatures are homogeneous within relevant solid angles. By adopting the expressions in [8] and [10], the satellite measured antenna temperature can be expressed to be

$$T_A^p = \xi_{Ref}^p [\eta_{me}^{pp} T_B^p + \eta_{me}^{qp} T_B^q + \eta_{se}^{pp} E_B^p + \eta_{se}^{qp} E_B^q + (\eta_{sc}^{pp} + \eta_{sc}^{qp}) T_C + (\zeta_{ss}^{pp} + \zeta_{ss}^{qp}) T_{SAT}] + (1 - \xi_{Ref}^p)\, T_{SAT}, \quad \text{(A2)}$$

where the instrument channel frequency υ and scan angle β are omitted in the equations for clarity; the superscript 'p' and 'q' represent the polarization status of the radiance or the antenna efficiencies, with p = 'v' for vertical polarization and 'h' for horizontal polarization. The explanation of each variable in (A2) is given in Table AI and the computation formulae of $\eta_x^{pp}, \eta_x^{qp}, \zeta_{ss}^{pp}$ and ζ_{ss}^{qp} are provided in [7] and are briefed in Section IV.B. In (A2), we assume that the temperature of the spacecraft associated with the item of $\left(1 - \xi_{Ref}^p\right)$ equal to that of the reflector with the item of $(\zeta_{ss}^{pp} + \zeta_{ss}^{qp})$, named to be T_{SAT} for clarity.

Table AI Explanations of variable used in (A2)

Variable	Explanations
T_A^p	Antenna temperature of the Earth scene at p-polarization illuminated by the main beam
T_B^p	Brightness temperature of the Earth scene at p-polarization illuminated by the main beam
E_B^p	Brightness temperatures of the Earth seen by the sidelobes
T_C	Brightness temperatures of the cold space seen by the sidelobes
T_{SAT}	Brightness temperature of the antenna on the satellite
η_x^{pp}	Co-polarized antenna efficiencies via a specific integration limit Ω_x subtended by the Earth (x=me or se) or cold space (x=sc)
η_x^{qp}	Cross-polarized antenna efficiencies via a specific integration limit Ω_x subtended by the Earth (x=me or se) or cold space (x=sc)
ζ_{ss}^{pp}	Co-polarized antenna efficiencies via a specific integration limit Ω_{ss} subtended by the spacecraft
ζ_{ss}^{qp}	Cross-polarized antenna efficiencies via a specific integration limit Ω_{ss} subtended by the spacecraft

The equation (A2) provides the formula of antenna temperature at vertical- or horizontal- polarization at a spaceborne microwave instrument. In practice, for a cross-track scanning microwave radiometer such as ATMS or AMSU-A, pure vertical- or horizontal- measurements only occur at the nadir direction. At the other scan angles (β), the measurements represent a mixed contribution from both V and H polarizations that is defined as the quasi-vertical and quasi-horizontal antenna brightness temperature respectively [8], i.e., $T_a^{Q_v}$ and $T_a^{Q_h}$.

For the convenience to derive $T_a^{Q_v}$ and $T_a^{Q_h}$, we re-arrange (A2) as

$$T_A^p = \xi_{Ref}^p[\eta_{me}^{pp}\, T_B^p + \eta_{me}^{qp}\; T_B^q + \eta_{se}^{pp}\, E_B^p + \eta_{se}^{qp}\, E_B^q + (\eta_{sc}^{pp} + \eta_{sc}^{qp})T_C] + S_A^p. \quad \text{(A3)}$$

with

$$S_A^p = \sigma\xi_{Ref}^p\left(\eta_{ss}^{pp} + \eta_{ss}^{qp}\right)T_{SAT} + \left(1.0 - \xi_{Ref}^p\right)T_{SAT} \quad \text{(A4)}$$

By inserting (A3) and (A4) into the following two equations for quasi-vertical and quasi-horizontal antenna brightness temperatures [8]

$$T_A^{Q_v} = T_A^v cos^2\theta + T_A^h sin^2\theta, \quad \text{(A5)}$$
$$T_A^{Q_h} = T_A^h cos^2\theta + T_A^v sin^2\theta, \quad \text{(A6)}$$

we have

$$T_A^{Q_v} = \xi_{Ref}^v[\eta_{me}^{vv}T_B^{Q_v} + \eta_{me}^{hv}T_B^{Q_h} + \eta_{se}^{vv}E_B^{Q_v} + \eta_{se}^{hv}E_B^{Q_h} + (\eta_{sc}^{vv} + \eta_{sc}^{hv})T_C] + S_a^{Q_v}, \quad \text{(A7)}$$

$$T_A^{Q_h} = \xi_{Ref}^h[\eta_{me}^{hh}T_B^{Q_h} + \eta_{me}^{vh}T_B^{Q_v} + \eta_{se}^{hh}E_B^{Q_h} + \eta_{se}^{vh}E_B^{Q_v} + (\eta_{sc}^{hh} + \eta_{sc}^{vh})T_C] + S_a^{Q_h} \quad \text{(A8)}$$

with

$$S_a^{Q_v} = C_0 + C_1\, sin^2\theta, \quad \text{(A9)}$$
$$S_a^{Q_h} = C_0 + C_1\, cos^2\theta, \quad \text{(A10)}$$
$$C_0 = \left[\sigma\xi_{Ref}^v(\eta_{ss}^{vv} + \eta_{ss}^{hv}) + \left(1.0 - \xi_{Ref}^v\right)\right]T_{SAT}, \quad \text{(A11)}$$
$$C_1 = \{\sigma(\xi_{Ref}^h\eta_{ss}^{hh} - \xi_{Ref}^v\eta_{ss}^{vv}) + \sigma\left(\xi_{Ref}^h\eta_{ss}^{vh} - \xi_{Ref}^v\eta_{ss}^{hv}\right) + \left(\xi_{Ref}^v - \xi_{Ref}^h\right)\}\, T_{SAT}. \quad \text{(A12)}$$

In the derivation of (A7) through (A12), we have $\xi_{Ref}^v \approx \xi_{Ref}^h$ and $\eta_x^{vv} \approx \eta_x^{hh}, with\ x = me\ or\ se\ or\ sc$ [8] for some of the simplifications.

Additionally, we defined the following relations [10]:

$$T_B^{Q_h}(\beta) = A^h(\beta)T_B^{Q_v}(\beta), \quad \text{(A13)}$$
$$T_B^{Q_v}(\beta) = A^v(\beta)T_B^{Q_h}(\beta), \quad \text{(A14)}$$

where $A^h(\beta)$ and $A^v(\beta)$ are empirical parameters describing the correlation between vertically and horizontally polarized Earth radiations.

Therefore, (A7) and (A8) are re-written to be

$$T_A^{Q_v} = \xi_{Ref}^v\{(\eta_{me}^{vv} + A^h\eta_{me}^{hv})T_B^{Q_v} + (\eta_{se}^{vv} + A^h\eta_{se}^{hv})E_B^{Q_v} + (\eta_{sc}^{vv} + \eta_{sc}^{hv})T_C + S_a^{Q_v}\}, \quad \text{(A15)}$$

$$T_A^{Q_h} = \xi_{Ref}^h\{(\eta_{me}^{hh} + A^v\eta_{me}^{vh})T_B^{Q_h} + (\eta_{se}^{hh} + A^v\eta_{se}^{vh})E_B^{Q_h} + (\eta_{sc}^{hh} + \eta_{sc}^{vh})T_C + S_a^{Q_h}\}, \quad \text{(A16)}$$

Alternatively,

$$T_A^{Q_v} = \xi_{Ref}^v\{[(\eta_{me}^{vv} + \eta_{se}^{vv}) + (\eta_{me}^{hv} + \eta_{se}^{hv})]T_B^{Q_v} + (\eta_{sc}^{vv} + \eta_{sc}^{hv})T_C + S_a^{Q_v}\} + (\Delta T_A^{Q_v})', \quad \text{(A17)}$$

$$T_A^{Q_h} = \xi_{Ref}^h\{[(\eta_{me}^{hh} + \eta_{se}^{hh}) + (\eta_{me}^{vh} + \eta_{se}^{vh})]T_B^{Q_h} + (\eta_{sc}^{hh} + \eta_{sc}^{vh})T_C + S_a^{Q_h}\} + (\Delta T_A^{Q_h})', \quad \text{(A18)}$$

with

$$(\Delta T_A^{Q_v})' = \xi_{Ref}^v\left[(A^h - 1.0)(\eta_{me}^{hv} + \eta_{se}^{hv})T_B^{Q_v} + (\eta_{se}^{vv} + \eta_{se}^{hv})(E_B^{Q_v} - T_B^{Q_v}) + (A^h - 1.0)\eta_{se}^{hv}(E_B^{Q_v} - T_B^{Q_v})\right], \quad \text{(A19)}$$

$$(\Delta T_A^{Q_h})' = \xi_{Ref}^h\left[(A^v - 1.0)(\eta_{me}^{vh} + \eta_{se}^{vh})T_B^{Q_h} + (\eta_{se}^{hh} + \eta_{se}^{vh})(E_B^{Q_h} - T_B^{Q_h}) + (A^v - 1.0)\eta_{se}^{vh}((E_B^{Q_h} - T_B^{Q_h})\right], \quad \text{(A20)}$$

Equation (A17) through (A20) represent generalized formulae of AMSU-A-measured antenna temperatures for a lossy antenna. It includes Earth radiation entering into the receiver system through the main beam and the sidelobes, the cold-space radiation through the sidelobes, the radiation emitted from satellite platform in the near-field through the sidelobes, as well as antenna emission. Additionally, it also contains the radiation perturbation due to the difference of Earth radiance in the main beam, and that in the sidelobes that lie outside the main beam but within the earth disc.

ACKNOWLEDGMENT

The authors would like to thank the NOAA Office of Projects, Planning, and Analysis (OPPA) for supporting Metop-C AMSU-A calibration/validation activities. Thank Dr. Phil Green for his providing Metop-C AMSU-A instrument measurement data and documentations. Thanks Dr. Robert Iacovazzi for his providing valuable comments and suggestions in reviewing the manuscript. The authors would also like to thank Dr. Ninghai Sun, Ms. Zhaohui Zhang, Dr. Junye Chen and Dr. Wenze Yang for their contributions to AMSU-A CRTM simulations. Thanks are extended to Drs. Changyong Cao, Cheng-zi Zou, and Haibing Sun for useful discussions and feedback. The last but not the least, the authors give sincere thanks to two anonymous reviewers for their many valuable comments.

REFERENCES

[1] Northrop Grumman Electronic Systems (NGES) technical report: Performance And Operation Specification for the Advanced Microwave Sounding Unit (POS), NASA GSFC-S-480-80 for AMSU-A1 S/N 105 through 109, 2010.

[2] Northrop Grumman Electronic Systems (NGES) technical report NAS 5-32314 CDRL 307, AMSU-A System Operation and Maintenance Manual for METSAT/METOP, S/N 105 through 109, 2010.

[3] J. P. Classen and A. K. Fung, "The recovery of polarized apparent temperature distributions of flat scenes from antenna temperature measurements," *IEEE Trans. Antennas Propagat.,* vol. AP-22, pp.433–442, May 1974.

[4] E. G. Njoku, "Antenna pattern correction procedures for the scanning multichannel microwave radiometer (SMMR)," *Boundary Layer Meteorol.,* vol. 18, pp.79–98, 1980.

[5] N. Grody, "Antenna temperature for a scanning microwave radiometer," *IEEE Trans. Antennas Propagat.,* vol. AP-28, pp.141–144, 1975.

[6] T. J. Hewsion and R. Saunders, "Measurements of the AMSU-B antenna pattern," *IEEE Trans. Geosci. Remote Sensing,* vol. 34, pp.405–412, 1996.

[7] T. Mo, "AMSU-A Antenna Pattern Corrections," I*EEE Trans. Geosci. Remote Sensing,* vol. 37, pp.103-112, 1999.
[8] F. Weng, H. Yang, and X. Zou, "On convertibility from antenna to sensor brightness temperature for advanced technology microwave sounder (ATMS)," *IEEE Geosci. Remote. Sens. Letter*, vol. 10, pp.771-775, 2013, [Online] Available: doi:10.1109/LGRS.2012.2223193
[9] Q. Liu, E. Kim, V. Leslie, and co-authors, "NOAA-20 ATMS TDR/SDR Validated Maturity Status Report," 2018, [Online] Available: https://www.star.nesdis.noaa.gov/jpss/documents/AMM/N20/ATMS_TDR_SDR_Validated.pdf
[10] F. Weng, X. Zou, N. Sun, and co-authors, "Calibration of Suomi national polar-orbiting partnership advanced technology microwave sounder," *J. Geophys. Res. Atmos.*, vol. 118, pp.1–14, 2013, [Online] Available: doi:10.1002/jgrd.50840
[11] F. Weng, "Passive Microwave Remote Sensing of the Earth: for Meteorological Applications," John Wiley & Sons, January, 2018
[12] H. Yang, F. Weng, and K. Anderson, "Estimation of ATMS Antenna Emission From Cold Space Observations," *IEEE Trans. Geosci. Remote Sens.,* vol. 54, pp. 4479-4487, 2016, [Online] Available: DOI:10.1109/TGRS.2016.2542526
[13] F. T. Ulaby and D. G., Long, "Microwave Radar and Radiometric Remote Sensing," ISBN 978-0-472-11935-6, University of Michigan Press, pp. 238 – 239, 2017.
[14] K. Ahmad and B. Yan, "AMSU-A Antenna Pattern Correction Algorithm Development and Validation," AGU Fall Meeting, Washington, D.C., Dec. 2018.
[15] Q. Liu and F. Weng, "Advanced Doubling-Adding Method for Radiative Transfer in Planetary Atmospheres," *J. Atmos. Sci.*, vol. 63, pp. 3459-3465, Dec. 2006.
[16] Y. Han, P. van Delst, Q. Liu, F. Weng, B. Yan, R. Treadon, and J. Derber, "JCSDA Community Radiative Transfer Model (CRTM) - Version 1," NOAA Tech. Rep. NESDIS 122, pp.1-33, 2006.
[17] S. Ding, P. Yang, F. Weng, Q. Liu, Y. Han, P. van Delst, J. Li, and B. Baum, "Validation of the community radiative transfer model," *J. Quant. Spectrosc. Radiat. Transfer*, vol. 112, pp. 1050-1064, Apr. 2011.
[18] "Calibration log book for the Advanced Microwave Sounding Unit-A (AMSU-A)", Report#10481A, Aerojet, Azusa, CA, Rep, 10481A, Sept., 1995
[19] M. Goldberg, M. D., S. Crosby, and L. Zhou, "The limb adjustment of AMSU-A observations," *J. Appl. Meteor.,* vol. 40, pp. 70–83, January 2001.
[20] B. Ingleby, "An assessment of different radiosonde types 2015/2016," ECMWF Technical Memoranda, 2017, [Online] Available: https://www.ecmwf.int/en/publications
[21] F. Carminat, S. Migliorini1, B. Ingleby, and coauthors, "Using reference radiosondes to characterise NWP model uncertainty for improved satellite calibration and validation," *Atmos. Meas. Tech., vol.* 12, pp.83–106, 2019, [Online] Available: https://doi.org/10.5194/amt-12-83-2019
[22] F. Weng, L. Zhao, R. Ferraro, G. Poe, X. Li, and N. Grody, "Advanced microwave sounding unit cloud and precipitation algorithms," *Radio Sci.,* 38, 8086–8096, 2003, [Online] Available: doi:10.1029/2002RS002679
[23] Q. Liu, F. Weng, and S. J. English, "An Improved Fast Microwave Water Emissivity Model," *IEEE Trans. Geosci. Remote Sens.,* vol. 49, pp. 1238-1250, 2011, [Online] Available: DOI: 10.1109/TGRS.2010.2064779
[24] B. Yan, J. Chen, C. Zou, K. Ahmad and H. Qian, "NOAA-20 Advanced Microwave Sounding Unit-A (AMSU-A) TDR/SDR Validated Maturity Status," NOAA Metop-C AMSU-A TDR/SDR Validated Maturity Review, August 2019.
[25] W. Yang, H. Meng, and R. Ferraro, "Cross-Scan Asymmetry of AMSU-A Window Channels: Characterization, Correction, and Verification," *IEEE Transactions on Geoscience and Remote Sensing, vol. 51,* pp.1514-1530, 2013, [Online] Available: DOI: 10.1109/TGRS.2012.2211884.

Banghua Yan received the Ph.D. degree in atmospheric physics from the Institute of Atmospheric Physics, Chinese Academy of Sciences, Beijing, China, in 1997 and the second Ph.D. degree in atmospheric physics from the University of Alaska, Fairbanks, in 2001. She is currently a physical scientist with the Satellite Calibration and Data Assimilation Branch in the NOAA Center for Satellite Applications and Research (STAR). From November 1999 to July 2010, she worked for the STAR through companies or NOAA Joint Center for Satellite Data Assimilation (JCSDA) or the Earth System Science Interdisciplinary Center in University of Maryland. During this period, she significantly contributed to the developments of microwave land, snow, and sea ice emissivity models, and microwave satellite instrument data assimilation studies. The land, snow, and sea ice microwave emissivity models had been implemented into the NOAA NCEP NWP model and the JCSDA community radiative transfer model. From August 2010 to August 2018, she was an Oceanographer with the NOAA Office of Satellite Data Processing and Distribution, Camp Springs, MD, to lead the NOAA operational ocean color production system. She has published over 20 papers in international peer-reviewed journals as the first or co-author. Currently, she leads the Metop-C AMSU-A and legacy microwave instrument calibration and validation (CalVal), the Joint Polar Satellite System (JPSS) Ozone Mapping and Profiler Suite (OMPS) CalVal, and the STAR Integrated Calibration/Validation System (ICVS). She also coordinates the JPSS/STAR (JSTAR) mission program.

Khalil Ahmad received the Ph.D. degree in electrical engineering from the Department of Electrical Engineering and Computer Science, University of Central Florida (UCF), Orlando, FL, USA in 2007. He was involved in the calibration/validation activities, and the development of wind vector cell rain flags for the NASA QuikSCAT/SeaWinds (QRad/SRad) Radiometers. In 2007, he joined NOAA/STAR to support the calibration/validation of various operational microwave scatterometer instruments, and evaluating their impacts on operational weather forecasting & warning environments. In 2011, he joined Raytheon Company, as a senior physics engineer, supporting the verification of IDPS system requirements, and evaluating the data quality of derived sensor products. In 2016, he returned back to NOAA/STAR, to support the calibration & validation work of operational microwave sounding instruments including the S-NPP/ATMS, and later the AMSU-A instrument onboard MetOp-C satellite. His primary efforts were focused on algorithm development & validation through sensor measurement simulation. He is currently a senior scientist with GST Inc., Greenbelt, MD, supporting the pre-launch & on-orbit calibration & validation activities of the Visible Infrared Imaging Radiometer Suite (VIIRS) sensors onboard operational & future JPSS satellite missions.